ROM SAF Report 31
Ref: SAF/ROM/METO/REP/RSR/031
Web: www.romsaf.org
Date: 7 May 2019

EUMETSAT
ROM SAF
RADIO OCCULTATION METEOROLOGY

ROM SAF Report 31

Sensitivity of some RO measurements to the shape of the ionospheric electron density profile

I D Culverwell

Met Office, Exeter, UK

Document Author Table

	Name	*Function*	*Date*	*Comments*
Prepared by:	I D Culverwell	ROM SAF Project Team	7 May 2019	
Reviewed by:	S Healy	ROM SAF review	23 Nov 2018	
Reviewed by:	M Forsythe, J Eyre	Met Office review	14 Jan 2019	
Reviewed by:	C Piccolo	Met Office approval	18 Apr 2019	
Approved by:	K B Lauritsen	ROM SAF Project Manager	7 May 2019	

Document Change Record

Issue/Revision	*Date*	*By*	*Description*
0.1	16 Mar 2018	IDC	1st version
0.2	19 Jul 2018	IDC	2nd version, tidying up App A
0.2	31 Dec 2018	IDC	3rd version, following review by SBH
0.3	18 Apr 2019	IDC	4th version, following review by Met Office
1.0	7 May 2019	IDC	Final version, following review by ROM SAF PM

ROM SAF

The Radio Occultation Meteorology Satellite Application Facility (ROM SAF) is a decentralised processing centre under EUMETSAT which is responsible for operational processing of GRAS radio occultation (RO) data from the Metop satellites and RO data from other missions. The ROM SAF delivers bending angle, refractivity, temperature, pressure, and humidity profiles in near-real time and offline for NWP and climate users. The offline profiles are further processed into climate products consisting of gridded monthly zonal means of bending angle, refractivity, temperature, humidity, and geopotential heights together with error descriptions.

The ROM SAF also maintains the Radio Occultation Processing Package (ROPP) which contains software modules that will aid users wishing to process, quality-control and assimilate radio occultation data from any radio occultation mission into NWP and other models.

The ROM SAF Leading Entity is the Danish Meteorological Institute (DMI), with Cooperating Entities: i) European Centre for Medium-Range Weather Forecasts (ECMWF) in Reading, United Kingdom, ii) Institut D'Estudis Espacials de Catalunya (IEEC) in Barcelona, Spain, and iii) Met Office in Exeter, United Kingdom. To get access to our products or to read more about the project please go to: http://www.romsaf.org

Intellectual Property Rights

Abstract

This report contains brief notes on the bending angles and slantwise total electron contents that result from the use of a single, spherically symmetric 'VaryChap' ionosphere. This is a simple but realistic model of the ionospheric electron density distribution whose shape can be easily altered. It is used to give some insight into the sensitivity of radio occultation results to the shape of the electron density profile.

Contents

1 Introduction

This report is an examination of the sensitivity of radio occultation measurements to the shape of the ionospheric electron density profile. This is done by calculating the bending angle and slantwise total electron content (STEC), both of which are measurable by radio occultation methods, generated by a spherically symmetric ionosphere whose electron density profile follows the so-called 'VaryChap' distribution. This is an asymmetrical distribution, characterised above its peak by an exponentially decreasing density whose e^{-1} decay length increases linearly with height ([1]). There is some recent observational support, based on COSMIC RO measurements, for the suggestion that the electron density above its peak can be modelled with a VaryChap electron density distribution ([5]). The important thing for our purposes is that a VaryChap layer is a physically reasonable model of ionospheric electron density, which has a simply parametrised shape, and which generates analytically tractable expressions for quantities that can be measured by radio occultation.

Usefully, the standard Chapman layer distribution is included in the family of VaryChap distributions, and (revised) results for this distribution are also recorded for completeness.

This study was made in response to the ionospheric products that the EPS-SG mission will attempt to deliver. These products will be based on measurements up to around 500 km. The ionosphere generally extends beyond this, and some degree of extrapolation will therefore be required if full ionospheric products are to be delivered. If the bending angles and/or STECs up to 500 km are sufficiently sensitive to the parameters of the VaryChap layer, then there is the hope that these parameters could be estimated by means of a variational retrieval. If so, then an estimate of the electron density at all heights would follow straightforwardly. This report is a first look at the feasibility of this hypothesis.

Note that the algebra in this report has not been thoroughly checked. Readers wanting to use any of the formulas contained within it would be well advised to carry out the calculations themselves. Please report any errors to the author via the ROM SAF helpdesk at http://www.romsaf.org.

2 Electron density distribution

In a so-called 'VaryChap' layer, the electron density scale height $H(r)$ increases linearly with distance above the peak r_0, thus:

$$H(r) = H_0 + k(r - r_0) \tag{2.1}$$

where $k = \partial H/\partial r > 0$ is constant. Evidently, $H_0 = H(r_0)$. As $k \to 0$ we recover the standard Chapman layer (Eqn A.1 in Appendix A), whose scale height is independent of distance. Note that there is no requirement that $r > r_0$ in Eqn 2.1. Thus, H decreases below the peak until it vanishes at $r = r_0 - H_0/k$.

Rishbeth and Garriott [1] use $H(r)$ to define a new vertical coordinate u, defined by $du/dr = H(r)^{-1}$, from which Eqn (2.1) implies, assuming we define u to be zero at $r = r_0$,

$$u(r) = k^{-1} \log\left(1 + \frac{k(r - r_0)}{H_0}\right), \tag{2.2}$$

$$\sim \frac{(r - r_0)}{H_0} + O(k) \quad \text{as } k \to 0. \tag{2.3}$$

Eqn (2.2) shows that $e^{ku} = H(r)/H_0$.

Substituting Eqn (2.2) into the basic equation (Rishbeth and Garriot 1969, Eqn 315) for the rate of electron production per unit volume, q, shows that

$$q \propto H(r)^{-1} \exp\left(1 - u - e^{-u}\right), \tag{2.4}$$

which implies that, at equilibrium, when $n_e^2 \propto q$ (because electron production then balances recombination, which can be taken to occur at a rate proportional to n_e^2 (e.g. [2])),

$$n_e(r) = n_e^{\max}(k) \exp\left[\frac{1+k}{2}\left(1 - \tilde{u} - e^{-\tilde{u}}\right)\right]. \tag{2.5}$$

In this equation $\tilde{u}$ is related to u via

$$\tilde{u} = u + \log(1+k). \tag{2.6}$$

The VaryChap layer Eqn (2.5) peaks at $\tilde{u} = 0$, which corresponds to

$$\frac{r - r_0}{H_0} = k^{-1}\left((1+k)^{-k} - 1\right) \tag{2.7}$$

$$\sim -k + O(k^2) \quad \text{as } k \to 0. \tag{2.8}$$

Since $k > 0$, this means that the VaryChap layer peaks below r_0, i.e. the place where $H(r) = H_0$.

The peak electron density, $n_e^{\max}(k)$ in Eqn (2.5) is not constant, but depends on k in the following way:

$$n_e^{\max}(k)/n_e^{\max}(0) = e^{-k/2}(1+k)^{(1+k)/2} \tag{2.9}$$

$$\sim 1 + k^2/4 + O(k^3) \quad \text{as } k \to 0. \tag{2.10}$$

(This disagrees with Rishbeth and Garriott [1], who say there's no dependence on k, but Eqn (2.9) follows directly from their Eqns 315 and 322. We suggest this is because Rishbeth and Garriott's scale height H appears to be constant below the peak height r_0, whereas our model H (Eqn 2.1) decreases below r_0.)

For the STEC and bending angle forward models, we would probably want to use $n_e^{\max}(0)$ as the variable, since in any retrieval that uses them we would hope to be able to ignore (at least intially) error correlations between (pairs of) ionospheric elements of the state vector.

The TEC is found by integrating the $n_e(r)$ in Eqn (2.5) with respect to r from $r_0 - H_0/k$ (where $H(r) = 0$) to ∞. We need $-1 < k < 1$ for the integral to converge, but in practice Olivares-Pulido *et. al.* [5] suggest $k \approx 0.1$, so this appears to be a safe assumption. We find

$$TEC = n_e^{\max}(0) H_0 \sqrt{e} 2^{(1-k)/2} \Gamma((1-k)/2) \tag{2.11}$$

$$\sim n_e^{\max}(0) H_0 \sqrt{2\pi e} \left[1 + \frac{k}{2}(\gamma + \log 2) + O(k^2) \right] \quad \text{as } k \to 0. \tag{2.12}$$

Here, $\gamma \approx 0.5772$ is the Euler-Mascheroni constant. Eqn 2.12 takes the right value (see Eqn (A.2) with $H = H_0$) at $k = 0$. And it agrees with numerically integrated TECs. Note that the TEC depends on k even if r_0 and H_0 are fixed.

Fig 2.1 shows various $n_e(r)$ profiles for VaryChap layers with some realistic values of k. The scale height above the peak appears to increase with k, as expected.

Fig 2.2 shows the variation with k of the TEC, the peak electron density and the peak height. As k goes from 0 to 0.2, the TEC increases by around 20%, the peak height falls by around $0.2H_0$ and the peak concentration hardly changes at all.

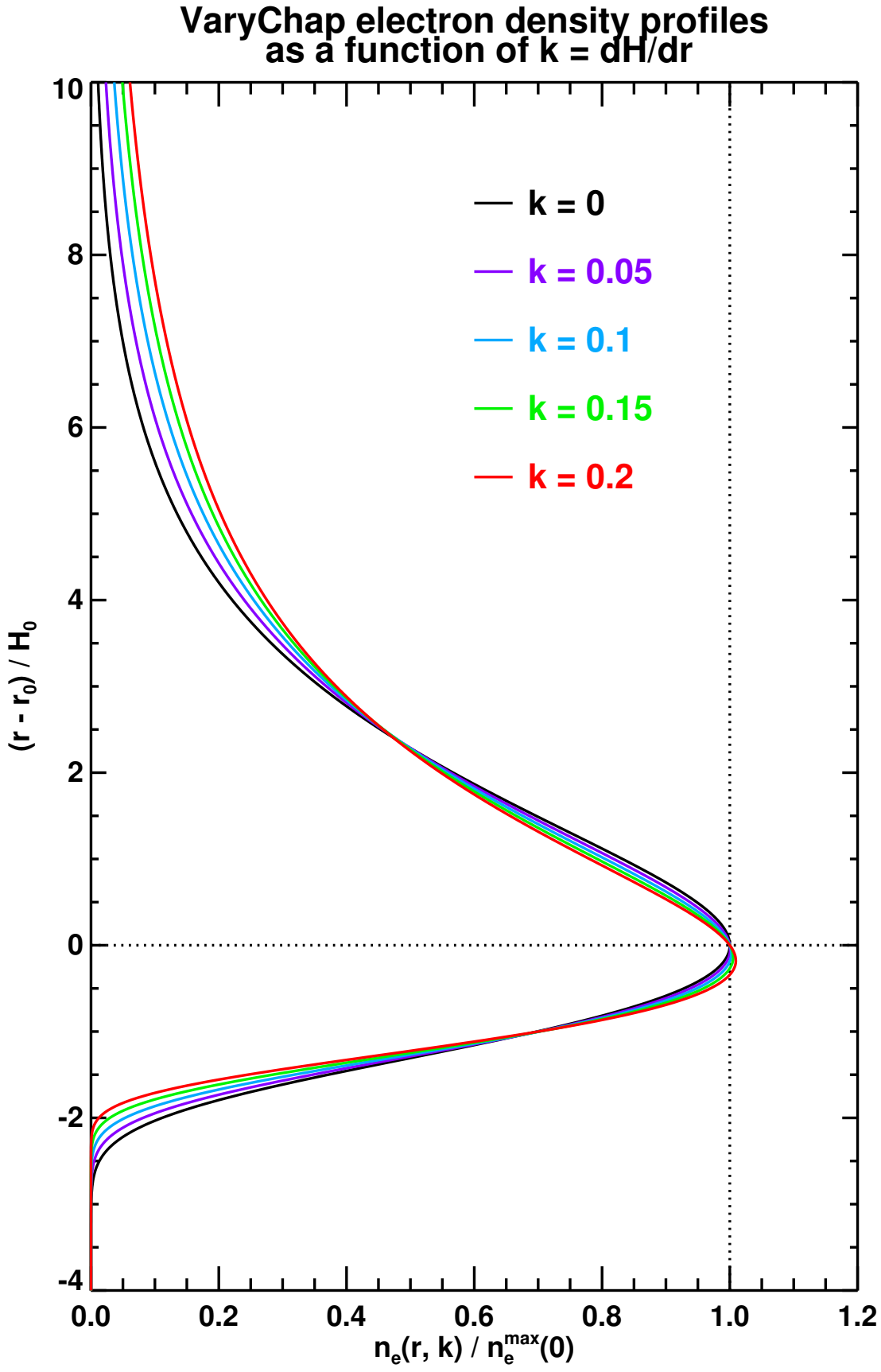

Figure 2.1: $n_e(r,k)/n_e^{\max}(0)$ given by Eqns (2.5) and (2.6) for realistic values of k.

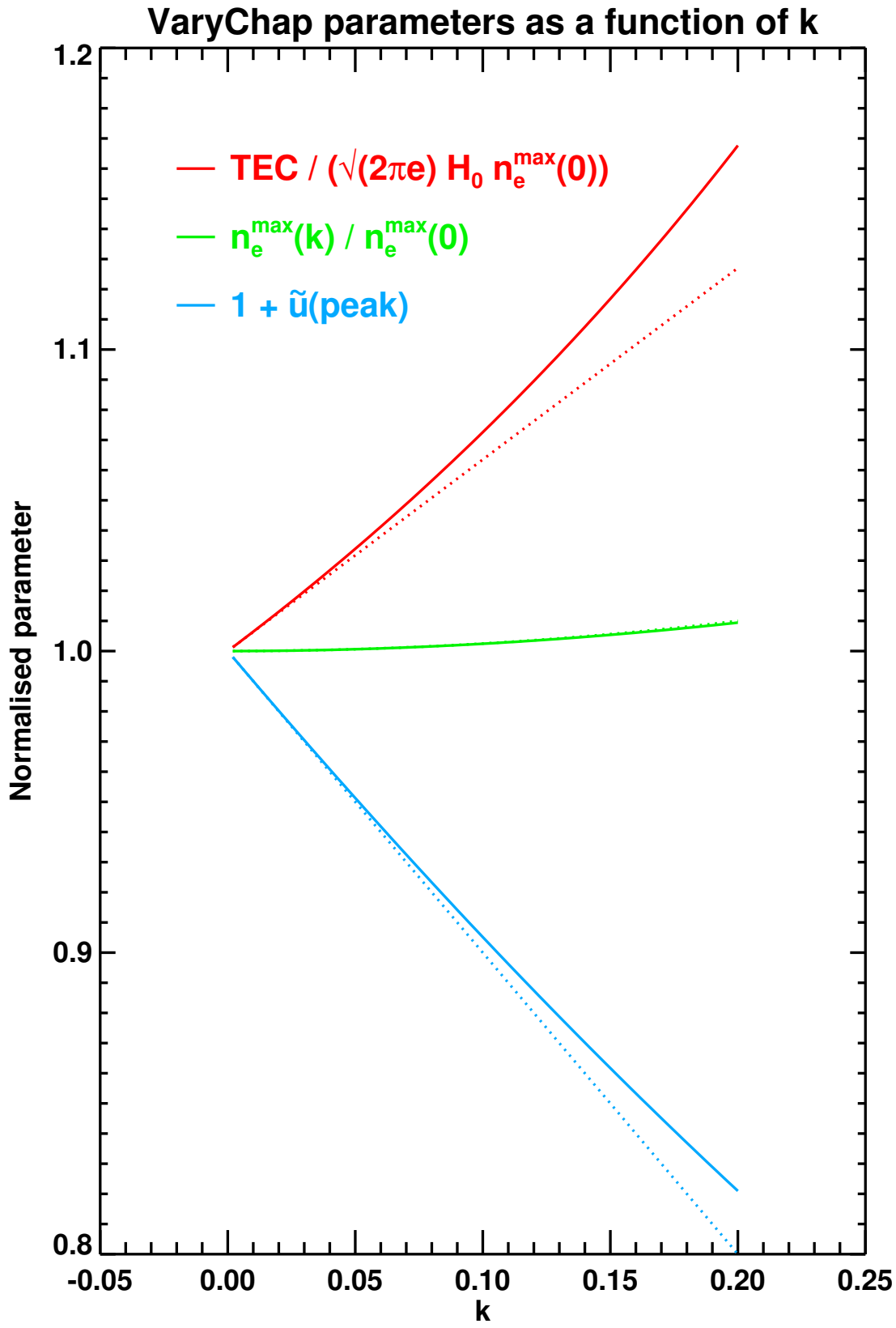

Figure 2.2: Variation with k of TEC, Eqn (2.11), peak electron density, Eqn (2.9), and peak height, Eqn (2.7). Dotted lines are the leading order approximations as $k \to 0$.

3 Bending angle

Substituting Eqn (2.5) in the basic bending angle integral (see Appendix A of RSR 17, [3]) shows that the generalised 'Zorro' function as a function of $k = \partial H/\partial r$ and l can be written as

$$\begin{aligned}
\tilde{Z}(k,l) &= (1+k)^{\frac{3+k}{2}} \int_{u_*}^{\infty} \left[\exp\left(-\frac{k+3}{2}\tilde{u}\right) - \exp\left(-\frac{k+1}{2}\tilde{u}\right) \right] \frac{\exp\left(-\frac{k+1}{2}e^{-\tilde{u}}\right) \mathrm{d}\tilde{u}}{\sqrt{k^{-1}(e^{k\tilde{u}}(1+k)^{-k} - 1 + kl)}} \qquad (3.1) \\
&= 2\int_{w_*}^{\infty} \left[\left(1 - kl + kw^2\right)^{-\frac{3k+3}{2k}} - (1+k)\left(1 - kl + kw^2\right)^{-\frac{3k+1}{2k}} \right] \\
&\times \exp\left(-(1/2)\left(1 - kl + kw^2\right)^{-\frac{1}{k}} \right) \mathrm{d}w, \quad \text{where } w^2 = k^{-1}\left(e^{k\tilde{u}}(1+k)^{-k} - 1 + kl\right) \qquad (3.2) \\
&\sim 2\sqrt{g}\int_0^{\infty} \left(g e^{-3w^2/2} - e^{-w^2/2} \right) \exp\left(-(g/2)e^{-w^2} \right) \mathrm{d}w \quad \text{as } k \to 0 \\
&= Z(l) \quad \text{as in Eqn (A.5).}
\end{aligned}$$

Here, $l = (r_0 - a)/H$ is the normalised distance below the peak of the Chapman layer, and $g = \exp(l)$. The lower limits of these bending angle integrals are defined by $(r_* - r_0)/H_0 = -k^{-1}$, where the scale height $H(r)$ vanishes. In terms of the independent variables $\tilde{u}$ and w in Eqns (3.1) and (3.2), this condition translates into (see Eqns (2.2) and (2.6))

$$\tilde{u}_* = k^{-1}\log\left[\max(1 - kl, 0)\right] + \log(1+k) \qquad (3.3)$$

and

$$w_*^2 = \max(l - k^{-1}, 0). \qquad (3.4)$$

The limit as $l' \to -\infty$ of $\tilde{Z}(k,l)$, for which $w_* = 0$, can be found by substituting $L = 1 - kl \to \infty$ in Eqn (3.2) to obtain

$$\begin{aligned}
\tilde{Z}(k,l) &= 2(1+k)^{\frac{3+3k}{2k}} \int_0^{\infty} \left[(1+k)^{-\frac{k+3}{2}} L^{-\frac{3+3k}{2k}} \left(1 + kw^2/L\right)^{-\frac{3+3k}{2k}} - (1+k)^{-\frac{1+k}{2}} L^{-\frac{1+3k}{2k}} \left(1 + kw^2/L\right)^{-\frac{1+3k}{2k}} \right] \\
&\times \exp\left(-(L^{-1/k}/2)\left(1 + kw^2/L\right)^{-1/k} \right) \mathrm{d}w \\
&\sim 2L^{-\frac{3+3k}{2k}} \int_0^{\infty} \left(1 + kw^2/L\right)^{-\frac{3+3k}{2k}} \mathrm{d}w - 2(1+k)L^{-\frac{1+3k}{2k}} \int_0^{\infty} \left(1 + kw^2/L\right)^{-\frac{1+3k}{2k}} \mathrm{d}w \quad \text{as } L \to \infty \qquad (3.5) \\
&= \sqrt{\frac{\pi}{k}} \left[(1-kl)^{-\frac{3+2k}{2k}} \frac{\Gamma((3+2k)/2k)}{\Gamma((3+3k)/2k)} - (1+k)(1-kl)^{-\frac{1+2k}{2k}} \frac{\Gamma((1+2k)/2k)}{\Gamma((1+3k)/2k)} \right]. \qquad (3.6)
\end{aligned}$$

By means of Stirling's approximation to the Gamma function, which shows that $\Gamma(z)/\Gamma(z+1/2) \sim z^{-1/2}$ as $z \to \infty$, we find that the last expression tends to $-\sqrt{2\pi g}$ as $k \to 0$, in agreement with Eqn (A.8). (The second term in Eqn (3.6) dominates in this limit because the first term is $O(g)$ ($\ll 1$) times as big.)

The limit as $l' \to \infty$ of $\tilde{Z}(k,l)$, for which $w_* = \sqrt{l - k^{-1}}$, can be found by substituting $v^2 = 1 - kl + kw^2$ in Eqn (3.2) to obtain

$$\tilde{Z}(k,l) = \frac{2}{k\sqrt{l}}\int_0^\infty \left[v^{-(3+2k)/k} - (1+k)v^{-(1+2k)/k}\right]\exp\left(-(1/2)v^{-2/k}\right)\frac{\mathrm{d}v}{\sqrt{1+(v^2-1)/kl}} \quad (3.7)$$

$$\sim \frac{2}{k\sqrt{l}}\int_0^\infty \left[v^{-(3+2k)/k} - (1+k)v^{-(1+2k)/k}\right]\exp\left(-(1/2)v^{-2/k}\right)\mathrm{d}v + O(l^{-1}) \text{ as } l\to\infty \quad (3.8)$$

$$= \frac{2}{\sqrt{l}}\int_0^\infty \left[(2y)^{(1+k)/2} - (1+k)(2y)^{(-1+k)/2}\right]e^{-y}\mathrm{d}y \quad (\text{where } y=(1/2)v^{-2/k}) \quad (3.9)$$

$$= \frac{2}{\sqrt{l}}\left[2^{(1+k)/2}\Gamma((3+k)/2) - (1+k)2^{(-1+k)/2}\Gamma((1+k)/2)\right] \quad (3.10)$$

$$= 0 \quad \text{exactly, since } \Gamma((3+k)/2) = ((1+k)/2)\Gamma((1+k)/2). \quad (3.11)$$

This makes sense: it amounts to integrating $\mathrm{d}n_e/\mathrm{d}r$ with respect to r in the original Abel integral, Eqn (A.4), without including the 'geometric' factor $(r^2-a^2)^{-1/2}$. It therefore gives $[n_e(r)]_a^\infty$, which equals 0 below the ionosphere. We therefore need to include the next term in the expansion of $(1+(v^2-1)/kl)^{-1/2}$ in Eqn (3.7), namely, $-(v^2-1)/2kl$. Using this in Eqn (3.8) gives[1]

$$\tilde{Z}(k,l) \sim \frac{-2}{2k^2\sqrt{l^3}}\int_0^\infty \left[v^{-(3+2k)/k} - (1+k)v^{-(1+2k)/k}\right](v^2-1)\exp\left(-(1/2)v^{-2/k}\right)\mathrm{d}v \text{ as } l\to\infty \quad (3.12)$$

$$= \frac{-1}{k\sqrt{l^3}}\int_0^\infty \left[(2y)^{(1-k)/2} - (1+k)(2y)^{(-1-k)/2}\right]e^{-y}\mathrm{d}y \quad (\text{where } y=(1/2)v^{-2/k}) \quad (3.13)$$

$$= \frac{-1}{k\sqrt{l^3}}\left[2^{(1-k)/2}\Gamma((3-k)/2) - (1+k)2^{(-1-k)/2}\Gamma((1-k)/2)\right] \quad (3.14)$$

$$= \frac{-2^{-(1+k)/2}}{k\sqrt{l^3}}\left[2\left((1-k)/2\right)\Gamma((1-k)/2) - (1+k)\,\Gamma((1-k)/2)\right] \quad (3.15)$$

$$= 2^{(1-k)/2}\,l^{-3/2}\,\Gamma((1-k)/2). \quad (3.16)$$

The last expression asymptotes to $\sqrt{2\pi/l^3}$ as $k\to 0$, in agreement with Eqn (A.10) ($l'/l\to 1$ as $l\to\infty$).

Fig 3.1 shows the generalised Zorro function, calculated numerically from Eqn (3.2), for various values of k. Also shown are the leading order asymptotic formulas Eqn (3.6), valid as $l'\to-\infty$, which can be seen to be reasonably accurate for $l'<-5$, and Eqn (3.16), valid as $l'\to\infty$, which is pretty poor even for $l=10$. It does have roughly the right shape, however.

In view of the closeness of the bending angle curves in Fig 3.1 there would seem to be little hope of learning something about the value of k by the use of bending angles in the usual range $3\lesssim l\lesssim 10$. There therefore seems little point in trying to develop (Padé?) approximations to $\tilde{Z}(k,l)$.

[1] Note that the -1 element of (v^2-1) in Eqn(3.12) also makes zero contribution, for the same reasons as above.

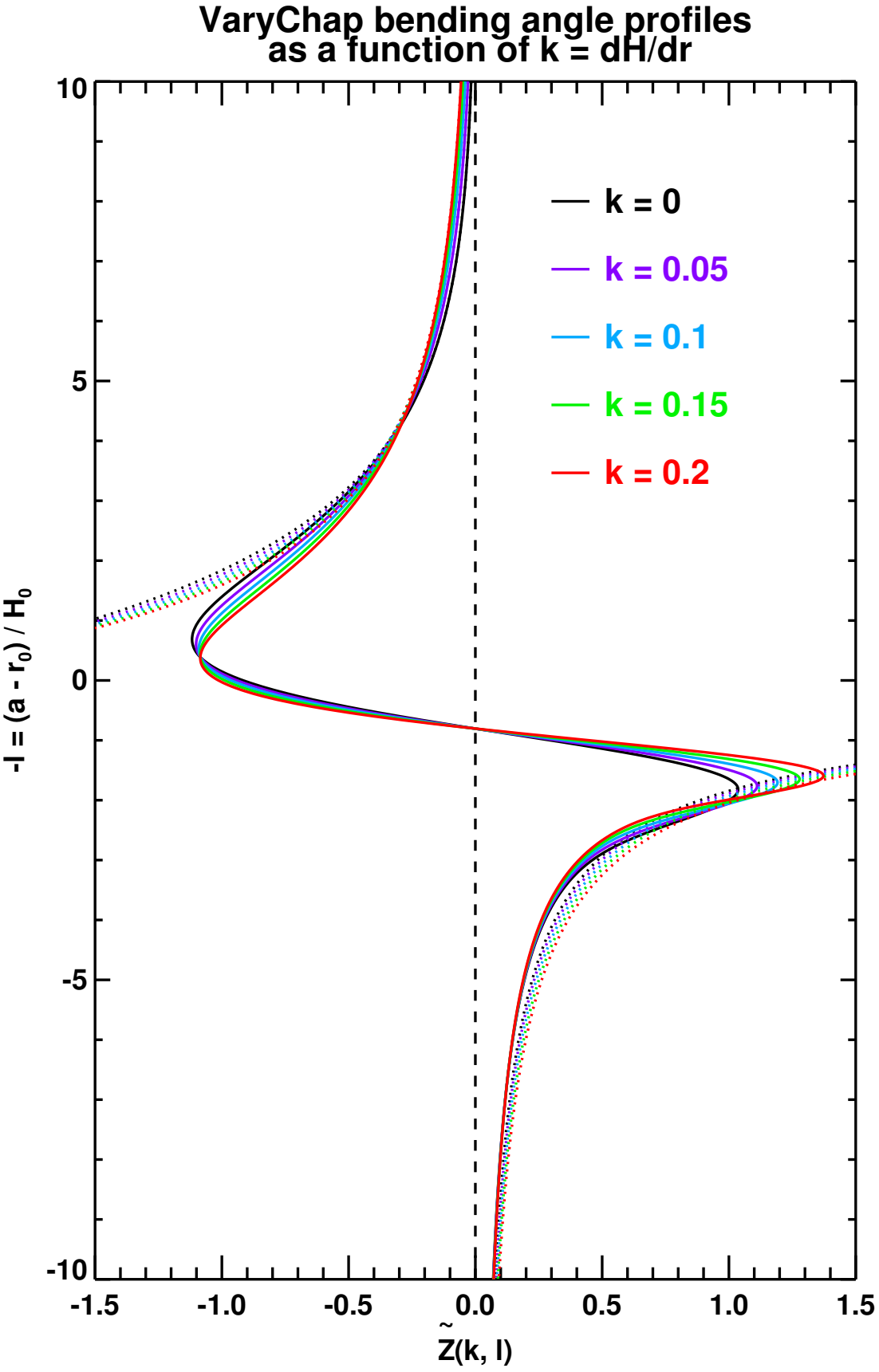

Figure 3.1: Variation with k of $\tilde{Z}(k,l)$, calculated numerically from Eqn (3.2). Also shown are the leading order asymptotic approximations as $l' \to -\infty$, Eqn (3.6), and as $l' \to \infty$, Eqn (3.16).

4 Slantwise TEC

Assuming a straight line path between LEO and GNSS, we find the slantwise total electron content, STEC, at impact height a, between two satellites at infinity, to be given by

$$\begin{aligned} STEC(a) &= 2\int_a^\infty n_e(r)\frac{r}{\sqrt{r^2-a^2}}\,\mathrm{d}r && (4.1)\\ &\approx 2\frac{r_0}{\sqrt{r_0+a}}\int_a^\infty n_e(r)\frac{1}{\sqrt{r-a}}\,\mathrm{d}r && (4.2)\\ &= 2r_0\,n_e^{\max}\sqrt{\frac{eH}{r_0+a}}\,\tilde{P}(k,l'), \quad \text{say.} && (4.3)\end{aligned}$$

In the above, $r/\sqrt{r^2-a^2}$ has been approximately factorised as $r_0/\left(\sqrt{r_0+a}\sqrt{r-a}\right)$ to ensure that Eqns (4.1) and (4.2) take the same value for a 'thin' ionosphere, defined by $n_e(r) = TEC\,\delta(r-r_0)$, which is an appropriate limit for this problem.

Substituting Eqn (2.5) into Eqn (4.2) shows that the generalised 'Pimpernel' function as a function of $k = \partial H/\partial r$ and l is given by

$$\begin{aligned} \tilde{P}(k,l) &= (1+k)^{\frac{1-k}{2}}\int_{u_*}^\infty \frac{\exp\left(-\frac{1-k}{2}\tilde{u}-\frac{k+1}{2}e^{-\tilde{u}}\right)\mathrm{d}\tilde{u}}{\sqrt{k^{-1}(e^{k\tilde{u}}(1+k)^{-k}-1+kl)}} && (4.4)\\ &= 2\int_{w_*}^\infty \left(1-kl+kw^2\right)^{-\frac{k+1}{2k}}\exp\left(-(1/2)\left(1-kl+kw^2\right)^{-\frac{1}{k}}\right)\mathrm{d}w && (4.5)\\ &\qquad \text{where } w^2 = k^{-1}\left(e^{k\tilde{u}}(1+k)^{-k}-1+kl\right)\\ &\sim 2\sqrt{g}\int_0^\infty \exp\left(-\frac{1}{2}w^2-\frac{g}{2}e^{-w^2}\right)\mathrm{d}w \quad \text{as } k\to 0\\ &= P(l) \quad \text{in Eqn (A.26).}\end{aligned}$$

The lower limits of these STEC integrals are as defined in Eqns (3.3) and (3.4).

The limit as $l'\to-\infty$ of $\tilde{P}(k,l)$, for which $w_* = 0$, can be found by substituting $L = 1-kl\to\infty$ in Eqn (4.5) to obtain

$$\begin{aligned} \tilde{P}(k,l) &= 2L^{-\frac{k+1}{2k}}\int_0^\infty \left(1+kw^2/L\right)^{-\frac{k+1}{2k}}\exp\left(-(L^{-1/k}/2)\left(1+kw^2/L\right)^{-1/k}\right)\mathrm{d}w && (4.6)\\ &\sim 2L^{-\frac{k+1}{2k}}\int_0^\infty \left(1+kw^2/L\right)^{-\frac{k+1}{2k}}\mathrm{d}w \quad \text{as } L\to\infty, \text{ assuming } k>0 && (4.7)\\ &= \sqrt{\frac{\pi}{k}}(1-kl)^{-\frac{1}{2k}}\frac{\Gamma(1/2k)}{\Gamma((k+1)/2k)}. && (4.8)\end{aligned}$$

Stirling's approximation to the Gamma function shows that the last expression asymptotes to $\sqrt{2\pi g}$ as $k\to 0$, in agreement with Eqn (A.28).

If we try to extend the utility of this result by expanding the exponential in Eqn (4.6) and integrating term-by-term, we end up with a series of increasingly large and oscillatory terms, which proves to be impossible to sum numerically beyond $l = 4.2$ for $k = 0$, and $l = 2.6$ for $k = 0.2$. This is not far enough, as l could be as small as 3 for a thick ionospheric F-layer.

The limit as $l' \to \infty$ of $\tilde{P}(k,l)$, for which $w_*^2 = l - k^{-1}$, can be found by substituting $v^2 = 1 - kl + kw^2$ in Eqn (4.5) to obtain

$$\tilde{P}(k,l) = \frac{2}{k\sqrt{l}} \int_0^\infty v^{-1/k} \exp\left(-(1/2)v^{-2/k}\right) \frac{\mathrm{d}v}{\sqrt{1+(v^2-1)/kl}} \tag{4.9}$$

$$\sim \frac{2}{k\sqrt{l}} \int_0^\infty v^{-1/k} \exp\left(-(1/2)v^{-2/k}\right) \mathrm{d}v + O(l^{-1}) \quad \text{as } l' \to \infty \tag{4.10}$$

$$= 2^{(1-k)/2}\, l^{-1/2}\, \Gamma((1-k)/2) \quad \text{(after substituting } y = (1/2)v^{-2/k}\text{)}. \tag{4.11}$$

The last expression asymptotes to $\sqrt{2\pi/l}$ as $k \to 0$, in agreement with Eqn (A.29) ($l'/l \to 1$ as $l \to \infty$).

Fig 4.1 shows the generalised Pimpernel function, calculated numerically from Eqn (4.5), for various values of k. Also shown are the leading order asymptotic expansions, Eqns (4.8) and Eqn (4.11). The first can be seen to be a good approximation five or more scale heights above the electron density peak. The second is less good, although it captures the trends in l and k below the peak.

There is a decent spread (up to a factor of ten) in the STECs above the peak as k goes from 0 to 0.2. This is far greater than the error in the forward model of a few per cent, which suggests that it might be possible to infer something about k from analysis of observed STECs (i.e. excess phase delays). How much of the information in the profile shape might be interpreted in terms of the other parameters — $n_e^{\max}(0), H_0$ etc — is unclear. It could be worth investigating. To do so would require, in a 1DVAR context, an expression for $\tilde{P}(k,l)$ that could be used in a forward model. One could numerically integrate Eqn (4.3) directly, but an approximate form might be quicker and accurate enough. We develop a first such approximation here.

Eqns (4.8) and (4.11) give the limiting form of $\tilde{P}(k,l)$ for large negative and positive l' respectively. By combining their fourth powers 'reciprocally', thus

$$\tilde{P}_0(k,l) = \left[\frac{\left(\sqrt{\frac{\pi}{k}}(1-kl)^{-\frac{1}{2k}} \frac{\Gamma(1/2k)}{\Gamma((k+1)/2k)}\right)^4 \left(\sqrt{\frac{2^{1-k}}{l}}\Gamma((1-k)/2)\right)^4}{\left(\sqrt{\frac{\pi}{k}}(1-kl)^{-\frac{1}{2k}} \frac{\Gamma(1/2k)}{\Gamma((k+1)/2k)}\right)^4 + \left(\sqrt{\frac{2^{1-k}}{l}}\Gamma((1-k)/2)\right)^4} \right]^{1/4}, \tag{4.12}$$

we have an expression, valid for all l, that conforms to these limits. In fact, Eqn (4.8) is only valid for $l < k^{-1}$, while Eqn (4.11) is only valid for $l > 0$, so that Eqn (4.12) is only applicable in the overlap region $0 < l < k^{-1}$. Outside this range, $\tilde{P}_0(k,l)$ equals whichever asymptotic form, Eqn (4.8) or (4.11), is valid. (In other words, we replace an invalid value with an infinite value in Eqn (4.12).) The jump in form of the function at $l = 0$ is responsible for the power $p = 4$ appearing in Eqn (4.12). Using the natural choice $p = 1$ leads to a cusp in $\tilde{P}_0(k,l)$ at $l = 0$, at least as $k \to 0$. $p = 2$ is continuous at $l = 0$ but not differentiable there; $p = 3$ is differentiable once; while $p = 4$ is differentiable twice (again, at least as $k \to 0$), which is desirable in something that could be used in a tangent linear or adjoint code.

The 'hybrid' expression $\tilde{P}_0(k,l)$ in Eqn (4.12), is included in Fig 4.1. It can be seen to exceed $\tilde{P}(k,l)$ in Eqn (4.3) by no more than about 50% in the range $-10 < l < 10$. We therefore make a Padé approximation to this ratio (minus one), thus

$$\frac{\tilde{P}(k,l)}{\tilde{P}_0(k,l)} - 1 \approx \frac{\sum_{i=0}^5 p_i(k)\theta^i}{\sum_{i=0}^5 q_i(k)\theta^i}, \tag{4.13}$$

where $\theta = \sinh^{-1}(e^l/4), p_0 = 0, q_0 = 1$ and $p_5 = 0$. (By construction, $\tilde{P}(k,l)/\tilde{P}_0(k,l)$ tends to 1 as $l \to \pm\infty$ (i.e. as $\theta \to 0$ and ∞), which explains the choice of p_0 and p_5.)

Fig 4.2 shows the Padé coefficients p_0 to p_5 and q_0 to q_5, calculated for 10 values of k between 0 and 0.225. These coefficients are calculated by means of a non-linear least squares fitting procedure[1],

[1] The IDL subroutine `lmfit`.

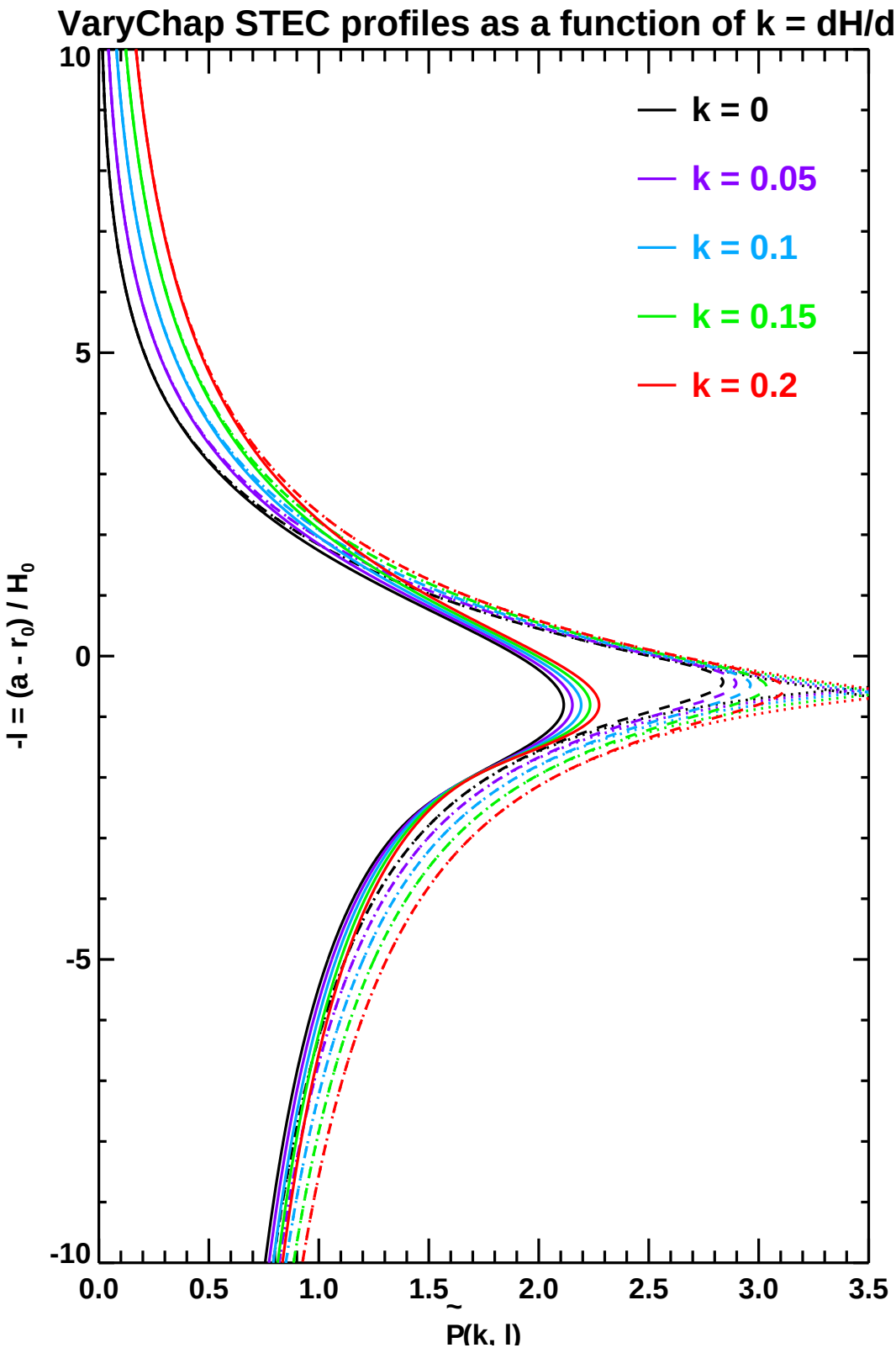

Figure 4.1: Variation with k of $\tilde{P}(k,l)$, calculated numerically from Eqn (4.5). Also shown (dotted lines) are the leading order asymptotic approximations as $l' \to -\infty$, Eqn (4.8), and as $l' \to \infty$, Eqn (4.11). The 'hybrid' function $\tilde{P}_0(k,l)$, Eqn (4.12), is also shown (dashed lines).

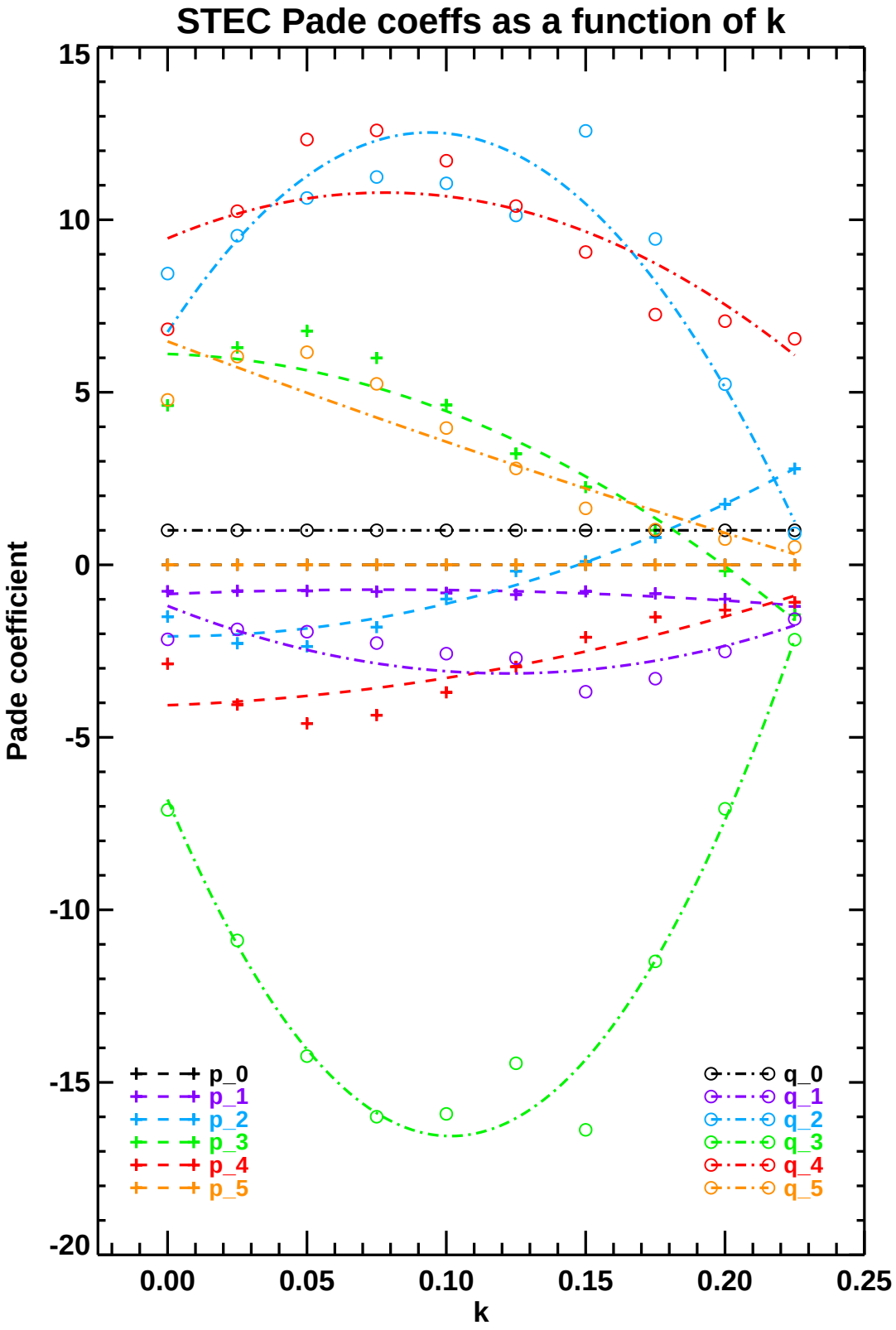

Figure 4.2: Coefficients in the Padé approximation to $\tilde{P}(k,l)$, Eqn (4.13), calculated (via a least squares fitting procedure) for 10 values of k. Also shown (dashed/dotted lines) are quadratic (in k) fits to those coefficients.

in which the initial estimates of $p_i(k)$ and $q_i(k)$ are found by demanding that the approximate curve matches the exact solution at selected values of l. 'Measurement errors' are taken to be proportional to $\sqrt{|l-l_0|}$, where $l_0 = 0.8047$ is the approximate location of the maximum of $P(0,l)$. This ensures a closer fit in the vicinity of the peak. (There is some sensitivity to these choices.) The resulting approximations to $\tilde{P}(k,l)$, and their fractional errors, are shown in Fig 4.3 for 5 values of k. The Padé approximations are clearly doing a reasonable job over this range of k and l.

Also shown in Fig 4.2 are quadratic approximations for the variation of $p_i(k)$ and $q_i(k)$ with k. In other words, we write

$$p_i(k) \approx p_i^{(0)} + p_i^{(1)}k + p_i^{(2)}k^2 \quad \text{for } i = 0,1,\ldots 5, \tag{4.14}$$

and similarly for $q_i(k)$. The coefficients in these fits, also found by a least squares fitting procedure[2], are given in Table 4.1. The quadratic approximations to $p_i(k)$ and $q_i(k)$ allow us to estimate $\tilde{P}(k,l)$ for any k and l, by combining Eqns (4.14), (4.13) and (4.12). The error in doing so, for a comprehensive range of k and l, is shown in Fig 4.4. It is within 2.0% everywhere, which is probably good enough for these purposes. As suggested by Fig 4.4, however, the approximations get worse as k increases, probably on account of the increasingly important k^2 term in Eqn (4.14). In any practical implementation of these ideas, 0.2 might need to be enforced as a hard upper limit on allowable k values. Similarly for 0.0 as a hard lower limit. (If k becomes negative, the scale height $H(r)$ vanishes above the peak, not below it, and many of the preceding calculations would need to be recomputed.)

Padé coefficients fitting parameters			
i	$p_i^{(0)}$	$p_i^{(1)}$	$p_i^{(2)}$
0	0.0000000000e+00	0.0000000000e+00	0.0000000000e+00
1	−8.4736594158e-01	3.2821051869e+00	−2.1106434130e+01
2	−2.0708259629e+00	−2.9209398857e-01	9.7343378388e+01
3	6.1101514241e+00	−2.3734170447e+00	−1.4187624752e+02
4	−4.0692658364e+00	2.9494359046e+00	4.9571873289e+01
5	0.0000000000e+00	0.0000000000e+00	0.0000000000e+00
i	$q_i^{(0)}$	$q_i^{(1)}$	$q_i^{(2)}$
0	1.0000000000e+00	0.0000000000e+00	0.0000000000e+00
1	−1.1897558009e+00	−3.2090937125e+01	1.3146993850e+02
2	6.7475341111e+00	1.2318502258e+02	−6.5608725220e+02
3	−6.8014209609e+00	−1.9207177935e+02	9.4540653413e+02
4	9.4595040317e+00	3.4032398902e+01	−2.1810139864e+02
5	6.4751678225e+00	−3.0456523559e+01	1.3565686782e+01

Table 4.1: Fits to Padé coefficients in Eqn (4.14).

[2]The IDL subroutine `poly_fit`.

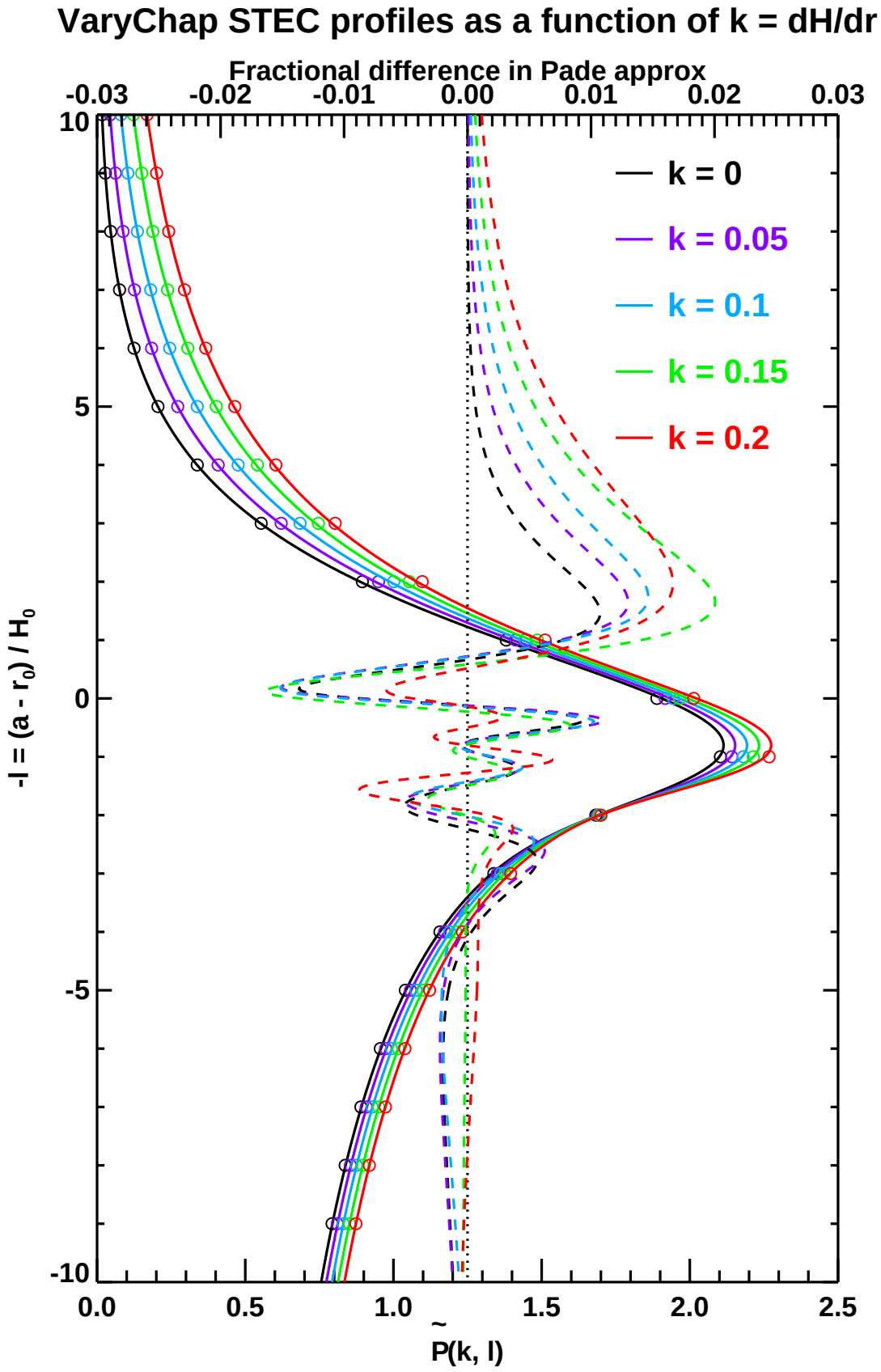

Figure 4.3: $\tilde{P}(k,l)$, Eqn (4.3), for a VaryChap layer, calculated numerically to high precision, for 5 values of k (solid lines). Also shown are the Padé approximations to $\tilde{P}(k,l)$, Eqn (4.13) (circles), and, with scale on the top axis, the fractional errors of these approximations (dashed lines).

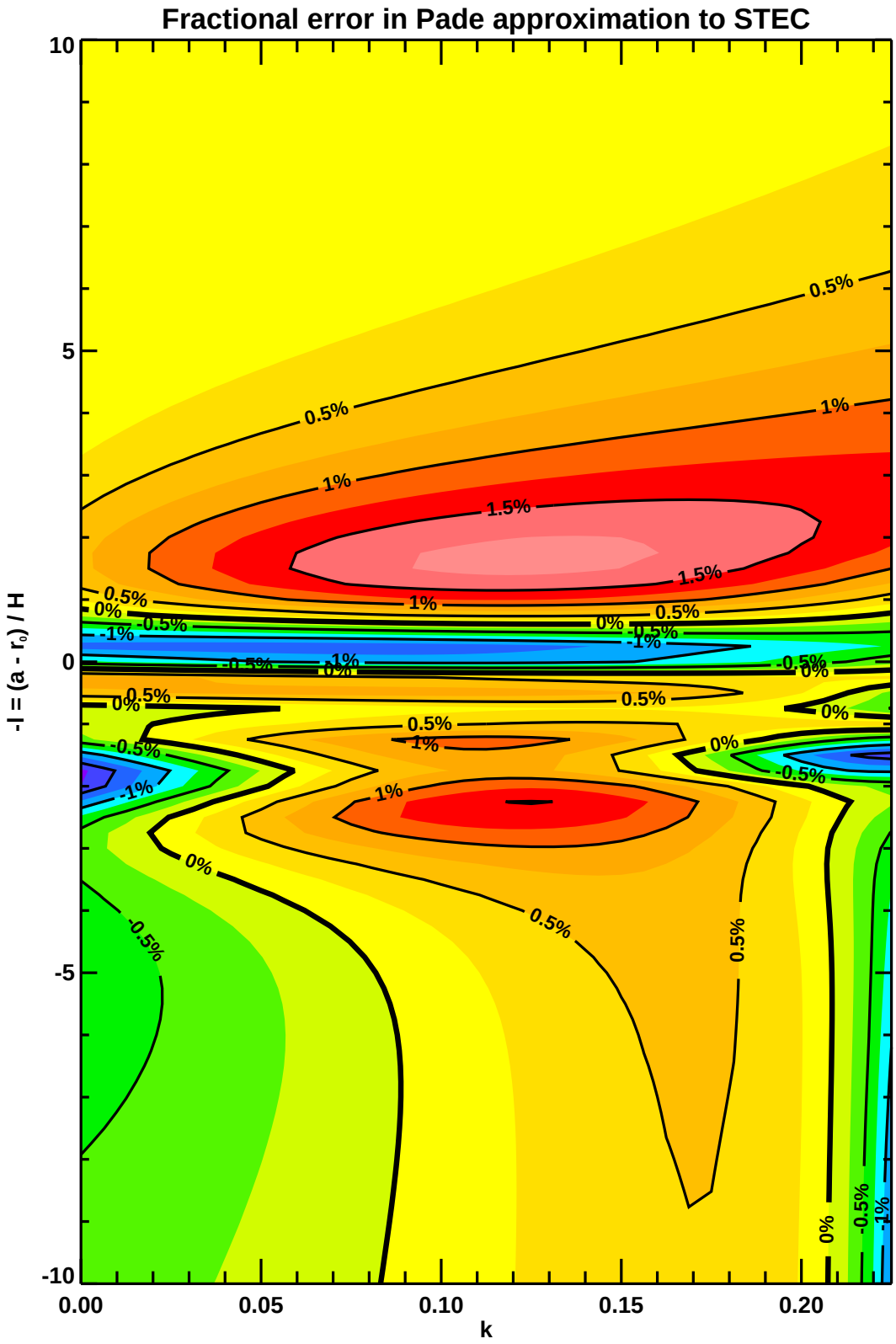

Figure 4.4: Fractional error in Eqn (4.13), using the coefficients calculated from Eqn (4.14) and the data in Table 4.1.

Direct numerical evaluation of Eqn (4.5), using Simpson's rule with 36 w-points between $w = w_*$ and $w = 10$ (a suitable maximum), also delivers a 2%-accurate solution. Its errors, however, oscillate systematically for large l, which may not be desirable (not shown). But even if we accept that limitation, the CPU time needed to do the numerical integration, even on such a coarse grid, is still over forty times that of the Padé approximations embodied by Eqns (4.14), (4.13) and (4.12). This is brought out in Fig 4.5, which compares the CPU times and accuracies of the 'exact' numerical integration, the 36-point Simpson's rule integration and the Padé approximation to $\tilde{P}(k,l)$. The trade-off between speed and accuracy in the various methods is clear. It also seems clear that need to take non-integral powers in Eqn (4.5) appreciably slows down the direct numerical integrations, because the $k = 0$ value, which uses different, analytically calculated formulas, is considerably faster. The Padé approximation suffers no such variation of CPU time with k.

Fig 4.5 shows that the Padé approximation delivers a speedy, tolerably accurate estimate the slant-wise TEC function $\tilde{P}(k,l)$. Simpson's rule with 36 points is slower but (usually) more accurate. In addition, the accuracy of the direct numerical integration can be improved by simply using a finer grid of w-points. Improving the accuracy of the Padé approximation would demand a lot of effort, with no guarantee of success.

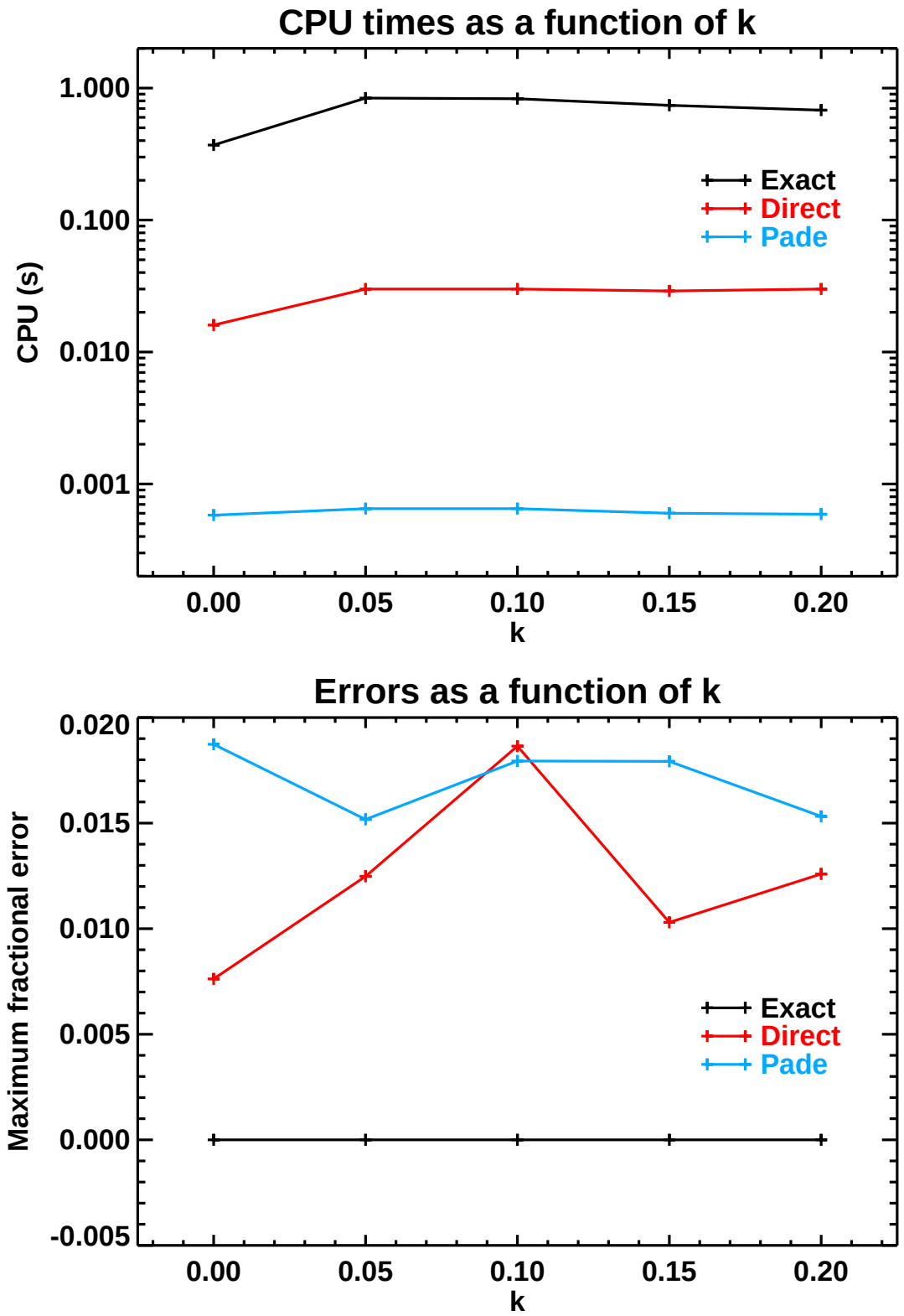

Figure 4.5: Top: CPU time for one evaluation (1000 l-values between -10 and 10) of $\tilde{P}(k,l)$ as a function of k for 'exact' numerical integration (the IDL routine `imsl_intfcn`), 'direct' numerical integration, using a 36-point Simpson's rule estimation, and the Padé approximation, Eqn (4.13). Bottom: Maximum errors, compared to exact integration, of the direct and Padé approximations, again as a function of k.

5 Summary, conclusions and future work

This report records some results, relevant to radio occultation, that follow from the assumption of a single, spherically symmetric 'VaryChap' layer ionosphere. The VaryChap electron density distribution has been defined and described. In this distribution the electron density scale height is a linearly increasing function of the height. This means that the scale height is larger than that of an equivalent Chapman layer above the peak and smaller beneath it. There is some experimental evidence ([5]) to suggest the existence of such ionospheric electron density profiles, at least above the peak.

The integrals defining the bending angles and slantwise total electron contents (STECs) of a VaryChap ionospheric layer have been calculated, and leading order asymptotic expressions for the behaviour far above and far below the electron density peak have been deduced. The bending angles show little variation with k, the gradient of the scale height with height, which suggests that there is little point in considering the generalised VaryChap distribution if we are only interested in investigating ionospheric corrections to bending angles below about 60 km. In these situations the standard Chapman layer model (e.g. RSR17 [2]) would suffice.

The STECs above the peak electron density, however, show greater variation with k — much greater than the uncertainty in the forward model — and this raises the possibility of using STEC measurements, which would be derived from excess phase observations, to infer something about this parameter of the VaryChap distribution, and, therefore, the entire electron density distribution.

A two per cent accurate approximation for the STEC as a function of k and l, the normalised distance below the ionospheric peak, has been provided in the form of a Padé approximation.

The bending angles and STECs for a 'standard' Chapman layer have been more extensively analysed. Padé approximations that are 1% accurate have been provided.

Future work in this area could include the following.

- A comparison of the STEC expressions in this report with observational data, to see if the latter allow any inferences to be drawn about the structure of the ionosphere — in particular, the gradient of its scale height with distance.
- The development of an approximation to the bending angle functions $\tilde{Z}(k,l)$, should it prove impossible to glean anything about electron density measurements from STEC measurements.
- A study of the impact of finite electron density at the LEO, which has been ignored in this work by assuming both satellites to be at infinity.

Acknowledgements

Extensive discussions on this subject with Sean Healy (ECMWF), and his careful review of the report, are gratefully acknowledged. Thanks are also extended to the other reviewers for their helpful comments.

A Appendix: 'Standard' Chapman layer results

A.1 Overview

This appendix records some results that follow from assuming a single, spherically symmetric Chapman layer ionosphere, which is a special case of a VaryChap layer in which the gradient of scale height, k, is zero.

Some of these results have already appeared in RSR 17 [3], but three aspects are new: an improved formula for the bending angles far below the ionosphere; an improved Padé approximation for the bending angles at all impact heights; and the analysis of the STEC for a Chapman layer.

A.2 Electron density

For a 'standard' Chapman layer the electron density is given by

$$n_e(r) = n_e^{\max} \exp\left(\frac{1}{2}\left(1-u-e^{-u}\right)\right) \tag{A.1}$$

where $u = (r-r_0)/H$, and $n_e^{\max}$ is the peak electron density, r_0 is the height of the peak, and H is a measure of the thickness of the Chapman layer. The total electron content (TEC) is found, by integrating the electron density over all heights, to be

$$TEC = \int_{-\infty}^{\infty} n_e(r)\,\mathrm{d}r = \sqrt{2\pi e}\, n_e^{\max} H. \tag{A.2}$$

A.3 Bending angles

Eqn A.7 of ROM SAF Report 17 shows that

$$\alpha_i(a) = \alpha(a, f_i) = \frac{k_4}{f_i^2} n_e^{max} \sqrt{\frac{4er_0^2a^2}{H(r_0+a)^3}}\, Z\left(\frac{r_0-a}{H}\right), \tag{A.3}$$

where the dimensionless, order 1, function Z is defined by

$$\begin{aligned} Z(l) &= \int_{-l}^{\infty} \frac{(e^{-3u/2} - e^{-u/2})\exp(-\frac{1}{2}e^{-u})}{\sqrt{u+l}}\,\mathrm{d}u & \text{(A.4)}\\ &= 2\sqrt{g}\int_0^{\infty}\left(ge^{-3w^2/2} - e^{-w^2/2}\right)\exp\left(-\frac{g}{2}e^{-w^2}\right)\mathrm{d}w, \quad \text{where } w^2 = u+l. & \text{(A.5)}\\ &= 2\sqrt{g}\left(gI_{3/2} - I_{1/2}\right), & \text{(A.6)} \end{aligned}$$

where

$$I_{n/2} = \int_0^{\infty} \exp\left(-\frac{n}{2}w^2 - \frac{g}{2}e^{-w^2}\right)\mathrm{d}w. \tag{A.7}$$

Here, u is as before, and $l = (r_0-a)/H$ is the H-normalised distance below the peak of the Chapman layer. g equals $\exp(l)$. In practice we are interested in $Z(l)$ for l between about 3 (for a broad F-layer) and about 10 (for a thin E-layer).

A.3.1 $l' \to -\infty$

Expanding the exponential and reversing the order of integration and summation leads, eventually (RSR 17, [3]), to

$$Z(l) = -2\sqrt{2\pi e^{l'}} \sum_{r=0}^{\infty} \frac{(-e^{l'})^r}{r!} \sqrt{r+1/2} \tag{A.8}$$

where $l' = l - \log 2$ (and $g' = g/2$). This is valid (convergent) for all l', but the oscillating and rapidly growing terms render it impossible to sum numerically if l' is greater than about 3. Euler summation helps a little, but not enough.

The first, second and 100th partial sums of Eqn (A.8) are shown in Fig A.1, as is the exact, numerically integrated solution.

A.3.2 $l' \to \infty$

Alternatively we can seek an expansion valid for large l'. Writing $s^2 = (1/2)\exp(-u)$ in the integrand of Eqn (A.4), and then expanding the radical, shows, eventually ([3]), that

$$\begin{aligned} Z(l) &\sim 2\sqrt{\frac{2}{l'}} \int_0^{\sqrt{g/2}} \frac{(2s^2-1)e^{-s^2}}{(1-2\log s/l')^{1/2}}\,\mathrm{d}s & \text{(A.9)} \\ &= 2\sqrt{\frac{2}{\pi l'^3}} \sum_{r=0}^{\infty} \frac{\Gamma(r+3/2)}{r!} \Gamma^{(r)}(1/2)(l')^{-r}. & \text{(A.10)} \end{aligned}$$

Here, $\Gamma(x) = \int_0^\infty t^{x-1}e^{-t}\mathrm{d}t$ is the usual Gamma function, and $\Gamma^{(r)}(1/2)$ is its r^{th} derivative at $x = 1/2$. Eqn (A.10) can be derived from Erdélyi and Olver's extension of Watson's lemma (RSR 17, App C, [3]).

The asymptotic expansion Eqn (A.10) is strongly divergent, and the first few terms are not accurate enough to be useful (RSR 17, [3]). This wild behaviour can be largely tamed by breaking the range of integration of Eqn (A.9) at $s = 1$. The first part can then be integrated by parts to yield

$$\begin{aligned} Z_1(l) &= 2\sqrt{\frac{2}{l'}} \int_0^1 \frac{(2s^2-1)e^{-s^2}}{(1-2\log s/l')^{1/2}}\,\mathrm{d}s & \text{(A.11)} \\ &= 2\sqrt{\frac{2}{l'}} \left\{ \left[\frac{-se^{-s^2}}{(1-2\log s/l')^{1/2}} \right]_0^1 + \frac{1}{l'} \int_0^1 \frac{e^{-s^2}}{(1-2\log s/l')^{3/2}}\,\mathrm{d}s \right\} & \text{(A.12)} \\ &= 2\sqrt{\frac{2}{l'}} \left\{ -e^{-1} + \sum_{r=0}^{\infty} \frac{(-1)^r}{r!} \left[1 - \sqrt{\pi(r+1/2)l'}\, e^{(r+1/2)l'} \operatorname{erfc}\left(\sqrt{(r+1/2)l'} \right) \right] \right\} & \text{(A.13)} \\ &= 2\sqrt{\frac{2}{l'}} \left\{ -e^{-1} + \frac{\sqrt{\pi}}{2l'} \operatorname{erf}(1) - \frac{3}{l'^2} \sum_{r=0}^{\infty} \frac{(-1)^r}{r!(2r+1)^2} \chi\left(\sqrt{(r+1/2)l'} \right) \right\} & \text{(A.14)} \end{aligned}$$

where the auxiliary function χ is defined as

$$\chi(x) = \frac{2x^2}{3}\left(1 - 2x^2 + 2\sqrt{\pi}x^3 \exp(x^2)\operatorname{erfc}(x)\right) \sim \begin{cases} 2x^2/3 + O(x^4) & \text{as } x \to 0 \\ 1 + O(x^{-2}) & \text{as } x \to \infty. \end{cases} \tag{A.15}$$

The boundedness of $\chi(x)$ as $x \to \infty$ and the rapidly increasingly denominator ensure that the series in Eqn (A.14) converges (absolutely) — and rather quickly. (Note that if we extend the upper limit of Eqn (A.11) to $\sqrt{g'} = \sqrt{g/2}$, we recover the unsummable Eqn (A.8).)

It remains to compute the tail of the integral, namely

$$Z_2(l) = 2\sqrt{\frac{2}{l'}}\int_1^{\sqrt{g'}} \frac{(2s^2-1)e^{-s^2}}{(1-2\log s/l')^{1/2}}\,\mathrm{d}s \tag{A.16}$$

$$= 2\sqrt{\frac{2}{l'}}\sum_{r=0}^{\infty}\frac{c_r}{l'^r}\int_1^{\sqrt{g'}}(-se^{-s^2})'\log^r s\,\mathrm{d}s, \quad \text{where } c_r=(2r)!/2^r(r!)^2 \tag{A.17}$$

$$= 2\sqrt{\frac{2}{l'}}\left\{\left[-se^{-s^2}\right]_1^{\sqrt{g'}} + \sum_{r=1}^{\infty}\left(\frac{c_r}{l'^r}\left[-se^{-s^2}\log^r s\right]_1^{\sqrt{g'}} + r\int_1^{\sqrt{g'}} e^{-s^2}\log^{r-1}s\,\mathrm{d}s\right)\right\} \tag{A.18}$$

$$\sim 2\sqrt{\frac{2}{l'}}\left\{e^{-1} + \frac{\sqrt{\pi}}{2l'}\mathrm{erfc}(1) + \sum_{r=2}^{\infty}\frac{c_r}{l'^r}I_r(g') + O\left(\sqrt{g'}e^{-g'}\right)\right\} \quad \text{as } l'\to\infty, \tag{A.19}$$

where

$$I_r(g') = r\int_1^{\sqrt{g'}} e^{-s^2}\log^{r-1}s\,\mathrm{d}s. \tag{A.20}$$

If $r \gg g'$ the integrand of I_r peaks beyond $s=\sqrt{g'}$, and we may estimate the value of I_r, using Laplace's method, to be $\sim \sqrt{g'}e^{-g'}(l'/2)^r r/(r-1)$ as $r\to\infty$. This would appear to give a divergent sum (terms going as $c_r/2^r$, the same as that of $(1-2x)^{-1/2}$ at $x=1/2$), but in fact I_r approximately cancels a term we have already ignored, namely the one that comes from $[-se^{-s^2}\log^r s]_1^{\sqrt{g'}}$ in Eqn (A.18), i.e. $-\sqrt{g'}e^{-g'}(l'/2)^r$. The two combine to make a series whose r^{th} term goes as $c_r/2^r(r-1)$, which is convergent ($\sum_{r=2}^{\infty}c_r/2^r(r-1)=1/2+\log 2$). In fact, the sum of this series beyond $r=[g']$ is approximately $(2/\sqrt{\pi})e^{-g'}$, which is negligible ('subdominant') compared to any inverse power of l'.

On the other hand, if $r \ll g'$, the integrand of I_r peaks below $s=\sqrt{g'}$, and Laplace's method shows that the difference between $I_r(\infty)$ and $I_r(g')$, namely $r\int_{\sqrt{g'}}^{\infty}e^{-s^2}\log^{r-1}s\,\mathrm{d}s$, is $\sim r(l'/2)^{r-1}e^{-g'}/2\sqrt{g'}$ as $g'\to\infty$. This subdominant difference means that we may replace $I_r(g')$ by $I_r(\infty)$ in the early terms of Eqn (A.19). These l'-independent coefficients can therefore be calculated (numerically) once and for all. The first ten are recorded in Table A.1. They get smaller at first, as the decreasing contribution from $\int_1^e \log^{r-1}s\exp(-s^2)\,\mathrm{d}s$ outweighs the increasing contribution from $\int_e^{\infty}\log^{r-1}s\exp(-s^2)\,\mathrm{d}s$, but the former tends to zero as r increases, and eventually, beyond $r=13$, the latter dominates and $I_r(\infty)$ starts to increase.

This large l' analysis breaks down if $l'\lesssim 2$, for then the $I_r(g')$ start off smaller than $I_r(\infty)$ (because the range of integration is small) and then rapidly decrease with r (because of the $(l'/2)^r$ behaviour noted above). $l'\approx 2$ (i.e. $l\approx 2.7$) is therefore a reasonable lower l'-limit for the validity of Eqn (A.19).

Combining Eqns (A.14) and (A.19) we find that

$$Z(l) = Z_1(l)+Z_2(l) \sim 2\sqrt{\frac{2}{l'}}\left\{\frac{\sqrt{\pi}}{2l'} - \frac{3}{l'^2}\sum_{r=0}^{\infty}\frac{(-1)^r}{r!(2r+1)^2}\chi\left(\sqrt{(r+1/2)l'}\right) + \sum_{r=2}^{\infty}\frac{c_r}{l'^r}I_r(\infty)\right\} \text{ as } l'\to\infty. \tag{A.21}$$

Note that Eqn (A.21) has the correct leading order behaviour for an infinitely thin 'delta function' ionosphere, namely

$$Z(l)\sim\sqrt{2\pi/l'^3} \quad \text{as } l'\to\infty. \tag{A.22}$$

The rapidly convergent series of χ functions in Eqn (A.21) is easily handled by direct summation. Including just the c_2I_2/l'^2 term of the second series gives a result which is within 2% for $l>2.7$. One iteration of Shanks' transformation/the Aitken δ^2-process (e.g. [4]) increases this accuracy to 2% for $l\approx 2.6$ and considerably better beyond. This provides our final expression for the large l' behaviour of $Z(l)$, which is therefore given by

$$Z(l)\sim 2\sqrt{\frac{2}{l'}}\left\{\frac{\sqrt{\pi}}{2l'} - \frac{3}{l'^2}\sum_{r=0}^{\infty}\frac{(-1)^r}{r!(2r+1)^2}\chi\left(\sqrt{(r+1/2)l'}\right) + \frac{c_2I_2}{l'^2} + \frac{c_3I_3/l'^3}{1-c_3I_3/c_2I_2l'}\right\} \text{ as } l'\to\infty. \tag{A.23}$$

Z_2 expansion coefficients		
r	c_r	$I_r(\infty)$
0	1.000000000e+00	3.678794411714423e-01 $(=e^{-1})$
1	1.000000000e+00	1.394027926403310e-01 $(=\sqrt{\pi}\,\mathrm{erfc}(1)/2)$
2	1.500000000e+00	7.176549918809735e-02
3	2.500000000e+00	4.339537686883779e-02
4	4.375000000e+00	2.922698909136269e-02
5	7.875000000e+00	2.133133448858963e-02
6	1.443750000e+01	1.659180176004288e-02
7	2.681250000e+01	1.360037129048910e-02
8	5.027343750e+01	1.165510151376709e-02
9	9.496093750e+01	1.037980864219113e-02

Table A.1: Z_2 expansion coefficients. $c_r = (2r)!/2^r(r!)^2$ and $I_r(\infty)$ is given by Eqn (A.20).

Eqn (A.23) is shown in Fig A.1, as is the exact, numerically integrated solution. The first and second partial sums of Eqn (A.10) are also plotted, which shows the improvements brought about by summing over χ functions and the use of Shanks' transformation.

A.3.3 All l'

Given the failings of the large- and small-l' approximations discussed above, an approximate numerical solution for all l' is necessary. The following Padé approximation is accurate to within 0.8% for $-10 < l < 30$ (except near the zero of Z, where the fractional error is understandably large):

$$Z(l) \approx \sqrt{2\pi\theta}\,\frac{\sum_{i=0}^{4} p_i\theta^i}{\sum_{i=0}^{6} q_i\theta^i} \quad \text{for all } l', \text{ where } \theta = \sinh^{-1}(g/4), p_0 = -2, q_0 = 1 \text{ and } p_4 = q_6, \tag{A.24}$$

for which the coefficients are given in Table A.2. (This expression is more accurate than the one described in RSR 17 ([3]), which is only correct to within 2.2%.)

Bending angle Padé coefficients	
p_0	−2.0000000000e+00 (=−2)
p_1	5.2266183047e+00
p_2	−3.2114861217e+00
p_3	7.7739693050e−01
p_4	9.5605233730e−02
q_0	1.0000000000e+00 (=1)
q_1	9.4886329835e−01
q_2	−1.0095779222e+00
q_3	2.9851107469e+00
q_4	−2.7624085011e+00
q_5	1.0987936603e+00
q_6	9.5605233730e−02 $(=p_4)$

Table A.2: Padé coefficients in Eqn (A.24)

Eqn (A.24), and its fractional difference from the numerically exact solution, is shown in Fig A.1.

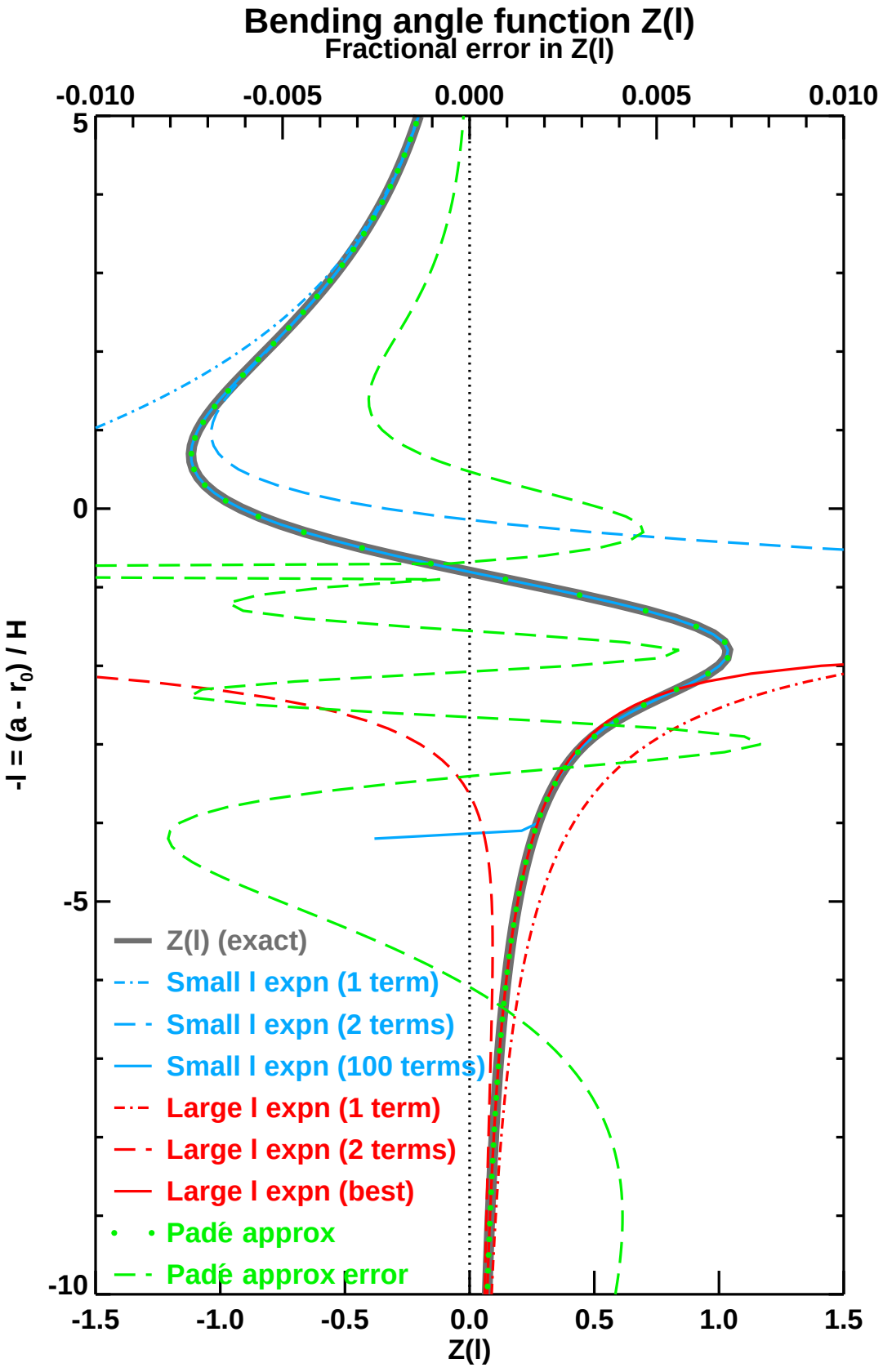

Figure A.1: $Z(l')$ for a Chapman layer, calculated numerically to high precision. Also shown are some partial sums of Eqn (A.8) (useful as $l' \to -\infty$), Eqn (A.23) and the first two partial sums of Eqn (A.10) (useful as $l' \to \infty$). Also shown is the Padé approximation Eqn (A.24) and its fractional error (useful for all l').

A.4 Slantwise TEC

For a Chapman layer electron density distribution Eqn (A.1), Eqn (4.3) in Sec 4 shows that

$$\tilde{P}(k,l) = \int_{-l}^{\infty} \frac{\exp -\frac{1}{2}(u+e^{-u})}{\sqrt{u+l}}\,\mathrm{d}u \quad (u=(r-r_0)/H;\, l=(r_0-a)/H) \tag{A.25}$$

$$= 2\sqrt{g}\int_0^{\infty} \exp -\frac{1}{2}\left(v^2+ge^{-v^2}\right)\mathrm{d}v \quad (v^2=u+l) \tag{A.26}$$

$$= P(l'), \quad \text{say.} \tag{A.27}$$

Using the same sorts of ideas as in Sec A.3, we find the 'Pimpernel' function, $P(l')$, for a Chapman layer ionosphere to be given by

$$P(l') \sim \sqrt{\pi g}\sum_{r=0}^{\infty}\frac{(-g/2)^r}{r!}(r+1/2)^{-1/2} = \sqrt{\pi g}\left(\sqrt{2}-g/\sqrt{6}+\ldots\right) \text{ as } l'\to-\infty \tag{A.28}$$

$$\sim \sqrt{2\pi/l'}\sum_{r=0}^{\infty}\frac{(-1/l')^r}{r!}\frac{\Gamma^{(r)}(1/2)}{\Gamma(1/2-r)} = \sqrt{2\pi/l'}\left(1-(\gamma+2\log 2)/2l'+\ldots\right) \text{ as } l'\to\infty \tag{A.29}$$

$$\approx \sqrt{2\pi\theta}\,\frac{\sum_{i=0}^{3}p_i\theta^i}{\sum_{i=0}^{4}q_i\theta^i} \quad \text{for all } l', \text{ where } \theta=\sinh^{-1}(g/4), p_0=2, q_0=1 \text{ and } p_3=q_4. \tag{A.30}$$

The Padé approximation in Eqn (A.30), using the coefficients given in Table A.3, is better than 1.0% accurate throughout the range -20 $\le l \le$ 30.

STEC Padé coefficients	
p_0	2.0000000000e+00 (=2)
p_1	−5.9759953854e−01
p_2	9.5873323918e−01
p_3	2.2033704905e−03
q_0	1.0000000000e+00 (=1)
q_1	8.8181359624e−01
q_2	2.6315962474e−01
q_3	9.6048213046e−01
q_4	2.2033704905e−03 (= p_3)

Table A.3: Padé coefficients in Eqn (A.30)

The exact, numerically integrated $P(l)$, the first two partial sums in both the large negative and the large positive l' expansions, and the Padé approximation and its fractional error, are plotted in Fig A.2. The general shape of $P(l)$ is clear: a maximum just below the peak of the Chapman layer (at $l=0$), where the ray intercepts a high number of electrons on its path. Below this, the gradually decreasing path length as the ray meets the ionosphere less and less tangentially, leads to a reduced STEC. Above it, where the ray skims through the top of the ionosphere, the STEC is also smaller. As the width of the Chapman layer tends to zero, Eqn (A.29) shows that $P(l')\sim\sqrt{2\pi/l'}$, which implies from Eqn (4.3) that

$$STEC \sim 2r_0\,n_e^{\max}\sqrt{\frac{eH}{r_0+a}}\sqrt{\frac{2\pi H}{r_0-a-H\log 2}} \tag{A.31}$$

$$\sim \frac{2r_0}{(r_0^2-a^2)^{1/2}}\sqrt{2\pi e}Hn_e^{\max}\left(=\frac{2r_0}{(r_0^2-a^2)^{1/2}}TEC\right) \quad \text{as } H\to 0 \tag{A.32}$$

which, by construction, is the correct limit, as can be verified by geometrical means.

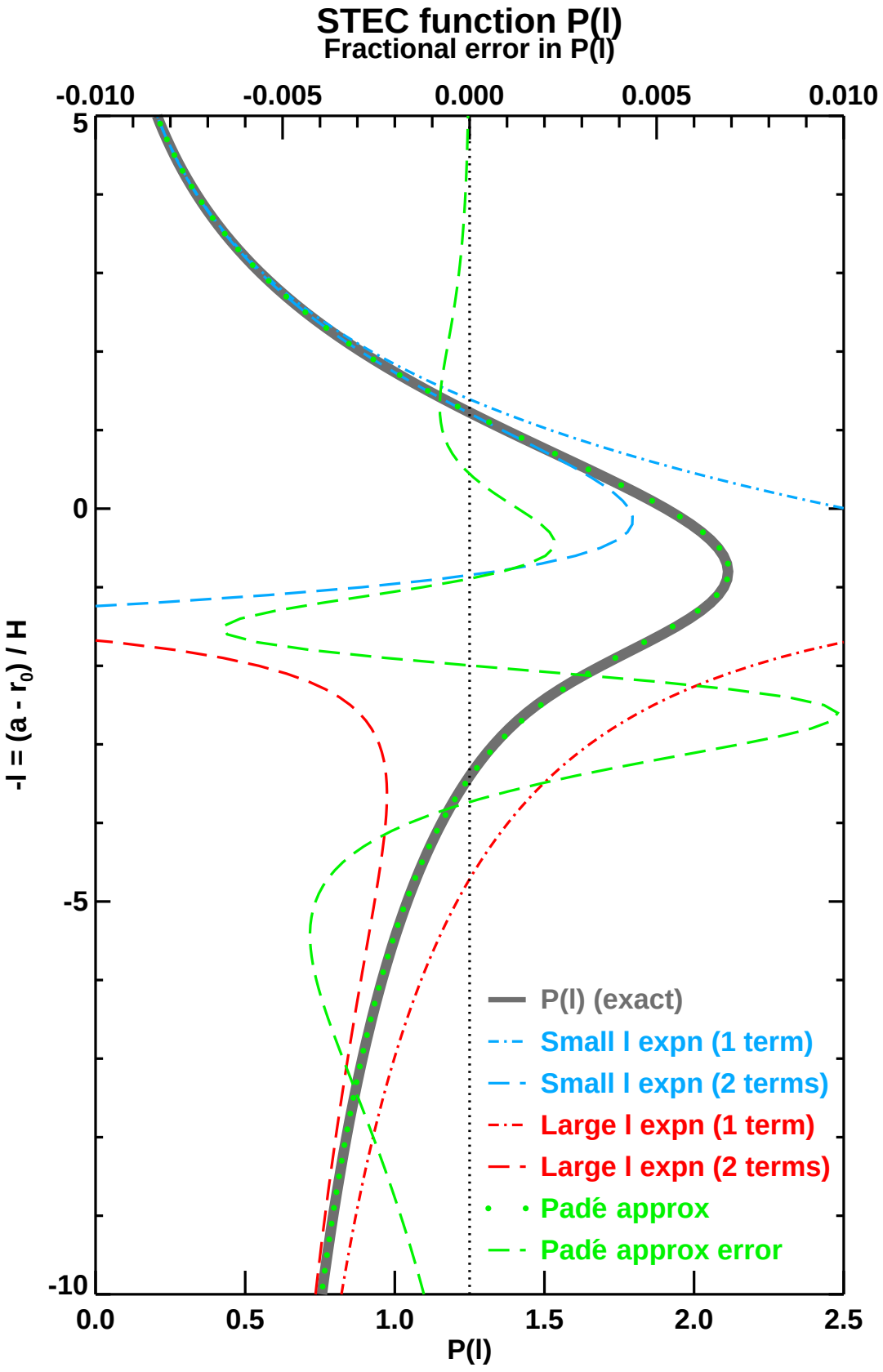

Figure A.2: $P(l')$ for a Chapman layer, calculated numerically to high precision. Also shown are the 1- and 2-term approximate expansions as $l' \to -\infty$, Eqn (A.28), and as $l' \to \infty$, Eqn (A.29). Also shown are the Padé approximation, Eqn (A.30), and, with its scale on the top axis, the fractional error on it.

Bibliography

[1] Rishbeth, H. and Garriott, O. K., Introduction to Ionospheric Physics, International Geophysics Series No. 14, Academic Press, 1969.

[2] Webber, W., The Production of Free Electrons in the Ionospheric D Layer by Solar and Galactic Cosmic Rays and the Resultant Absorption of Radio Waves, J. Geophys. Res., 67, No. 13, 5091–5106, 1962.

[3] Culverwell, I. D. and Healy, S. B., Simulation of L1 and L2 bending angles with a model ionosphere, ROM SAF Report 17, http://www.romsaf.org/general-documents/rsr/rsr_17.pdf, 2015.

[4] Mathews J and Walker R L, Mathematical Methods of Physics, 2nd Edition, W A Benjamin, 1970.

[5] Olivares-Pulido, G., M. Hernández-Pajares, A. Aragón-Angel, and A. Garcia-Rigo, A linear scale height Chapman model supported by GNSS occultation measurements, J. Geophys. Res. Space Physics, 121, 7932–7940, 2016. doi:10.1002/2016JA022337.

ROM SAF (and earlier GRAS SAF) Reports

SAF/GRAS/METO/REP/GSR/001	Mono-dimensional thinning for GPS Radio Occulation
SAF/GRAS/METO/REP/GSR/002	Geodesy calculations in ROPP
SAF/GRAS/METO/REP/GSR/003	ROPP minimiser - minROPP
SAF/GRAS/METO/REP/GSR/004	Error function calculation in ROPP
SAF/GRAS/METO/REP/GSR/005	Refractivity calculations in ROPP
SAF/GRAS/METO/REP/GSR/006	Levenberg-Marquardt minimisation in ROPP
SAF/GRAS/METO/REP/GSR/007	Abel integral calculations in ROPP
SAF/GRAS/METO/REP/GSR/008	ROPP thinner algorithm
SAF/GRAS/METO/REP/GSR/009	Refractivity coefficients used in the assimilation of GPS radio occultation measurements
SAF/GRAS/METO/REP/GSR/010	Latitudinal Binning and Area-Weighted Averaging of Irregularly Distributed Radio Occultation Data
SAF/GRAS/METO/REP/GSR/011	ROPP 1dVar validation
SAF/GRAS/METO/REP/GSR/012	Assimilation of Global Positioning System Radio Occultation Data in the ECMWF ERA-Interim Re-analysis
SAF/GRAS/METO/REP/GSR/013	ROPP PP validation
SAF/ROM/METO/REP/RSR/014	A review of the geodesy calculations in ROPP
SAF/ROM/METO/REP/RSR/015	Improvements to the ROPP refractivity and bending angle operators
SAF/ROM/METO/REP/RSR/016	Simplifying EGM96 undulation calculations in ROPP
SAF/ROM/METO/REP/RSR/017	Simulation of L1 and L2 bending angles with a model ionosphere
SAF/ROM/METO/REP/RSR/018	Single Frequency Radio Occultation Retrievals: Impact on Numerical Weather Prediction
SAF/ROM/METO/REP/RSR/019	Implementation of the ROPP two-dimensional bending angle observation operator in an NWP system
SAF/ROM/METO/REP/RSR/020	Interpolation artefact in ECMWF monthly standard deviation plots
SAF/ROM/METO/REP/RSR/021	5th ROM SAF User Workshop on Applications of GPS radio occultation measurements
SAF/ROM/METO/REP/RSR/022	The use of the GPS radio occultation reflection flag for NWP applications
SAF/ROM/METO/REP/RSR/023	Assessment of a potential reflection flag product
SAF/ROM/METO/REP/RSR/024	The calculation of planetary boundary layer heights in ROPP
SAF/ROM/METO/REP/RSR/025	Survey on user requirements for potential ionospheric products from EPS-SG radio occultation measurements

ROM SAF (and earlier GRAS SAF) Reports (cont.)

SAF/ROM/METO/REP/RSR/026	Estimates of GNSS radio occultation bending angle and refractivity error statistics
SAF/ROM/METO/REP/RSR/027	Recent forecast impact experiments with GPS radio occultation measurements
SAF/ROM/METO/REP/RSR/028	Description of wave optics modelling in ROPP-9 and suggested improvements for ROPP-9.1
SAF/ROM/METO/REP/RSR/029	Testing reprocessed GPS radio occultation datasets in a reanalysis system
SAF/ROM/METO/REP/RSR/030	A first look at the feasibility of assimilating single and dual frequency bending angles
SAF/ROM/METO/REP/RSR/032	An initial assessment of the quality of RO data from KOMPSAT-5
SAF/ROM/METO/REP/RSR/033	Some science changes in ROPP-9.1

ROM SAF Reports are accessible via the ROM SAF website: http://www.romsaf.org